

Viscous control of shallow elastic fracture: peeling without precursors

John R. Lister¹, Dominic J. Skinner^{1,2} and Timothy M. J. Large^{1,2}

¹Department of Applied Mathematics and Theoretical Physics, University of Cambridge, Wilberforce Road, Cambridge CB3 0WA, UK

²Department of Mathematics, Massachusetts Institute of Technology, Cambridge, MA 02139-4307, USA

(Received 11 February 2019; revised xx; accepted xx)

We consider peeling of an elastic sheet away from an elastic substrate through propagation of a fluid-filled crack along the interface between the two. The peeling is driven by a bending moment applied to the sheet and is resisted by viscous flow towards the crack tip and by the toughness of any bonding between the sheet and the substrate. Travelling-wave solutions are determined using lubrication theory coupled to the full equations of elasticity and fracture. The propagation speed v scales like $M^3/\mu\bar{E}^2d^5 = Bd\kappa^3/144\mu$, where d is the sheet's thickness, $B = \bar{E}d^3/12$ its stiffness, $\bar{E} = E/(1 - \nu^2)$ its plane-strain modulus, μ the fluid viscosity, M the applied bending moment and $\kappa = M/B$ the sheet's curvature due to bending; and the pre-factor depends on the dimensionless toughness. If the toughness is small then there is a region of dry shear failure ahead of the fluid-filled region. The expressions for the propagation speed have been used to derive new similarity solutions for the spread of an axisymmetric fluid-filled blister in a variety of regimes: constant-flux injection resisted by elastohydrodynamics in the tip leads to spread proportional to $t^{4/13}$, $t^{4/17}$ and $t^{7/19}$ for peeling-by-bending, gravitational spreading, and peeling-by-pulling, respectively.

1. Introduction

Viscous intrusion of fluid beneath an elastic sheet is controlled by the dynamics at the front, where the sheet is peeled away from the underlying substrate. Such coupling of the dynamics of viscous flow and sheet deformation has many and diverse applications. These include the geological formation and growth of laccoliths by magmatic intrusion at shallow depths (e.g. Michaut 2011; Bunge & Cruden 2011), the dilation of elastic-walled Hele-Shaw cells (Pihler-Puzović *et al.* 2012, 2015; Lister *et al.* 2013; Ducloué *et al.* 2017), cell adhesion and detachment (Hodges & Jensen 2002; Leong & Chiam 2010), peeling of adhesive tape (McEwan & Taylor 1966), growth of liquid blisters (Chopin *et al.* 2008; Peng *et al.* 2015), airway reopening (Jensen *et al.* 2002; Grotberg & Jensen 2004; Heil & Hazel 2011) and the manufacture of flexible electronics and microelectromechanical systems (Hosoi & Mahadevan 2004; Rogers *et al.* 2010; Gomez *et al.* 2017).

The simplest model for flow in a thin fluid layer of viscosity μ and thickness $h(x, y, t)$ beneath a stiff elastic sheet of uniform thickness d is obtained by substituting the pressure $p = B\nabla^4 h$ produced by bending stresses in the sheet into the Reynolds lubrication equation (e.g. Leal 1992) to obtain

$$\frac{\partial h}{\partial t} = \frac{B}{12\mu} \nabla \cdot (h^3 \nabla \nabla^4 h), \quad (1.1)$$

where $B = Ed^3/12(1 - \nu^2)$ is the bending stiffness of the sheet, E and ν are its Young's modulus and Poisson's ratio, and ∇ is the gradient operator in the x, y -plane.

The sixth-order equation (1.1) does not support solutions with a forwards propagating front at which $h = 0$ (Flitton & King 2004; Lister *et al.* 2013; Hewitt *et al.* 2015). In that respect, it is like the fourth-order thin-film equation for lubrication flows driven by a capillary pressure $p = -\sigma\nabla^2 h$, with surface tension σ , for which the so-called contact-line problem is often resolved by introducing a slip length or a prewetting film to model processes near the apparent contact line and regularize the equation (Hocking 1983; Hervet & de Gennes 1984). For a capillary-driven flow, the resulting contact-line speed depends only very weakly (logarithmically) on the details of this regularization (Bonn *et al.* 2009). However, for flow driven by elastic bending stresses, as described in the interior by (1.1), the speed of any propagating front is controlled by the peeling processes at the front, and the interior solution is then quasistatic with $\nabla p = \mathbf{0}$ at leading order.

Lister *et al.* (2013) considered the case where there is already a prewetting fluid film of some small thickness h_0 between the elastic sheet and the underlying substrate, as in recent experiments on blister growth in a pre-filled elastic-walled Hele-Shaw cell (Pihler-Puzović *et al.* 2012, 2015; Peng *et al.* 2015; Ducloué *et al.* 2017). A local travelling-wave analysis near the front shows that the edge of the blister spreads at a speed $v = (B^2 h_0 \kappa^5)^{1/2}/\mu$, where the curvature $\kappa = h''$ at the edge of the blister is determined by the quasistatic interior solution. Hewitt *et al.* (2015) considered an alternative situation where a precursor phase of low-viscosity vapour at some fixed pressure $-p_0$ occupies the tip of the propagating front (see also Ball & Neufeld 2018; Wang & Detournay 2018). This description, known as ‘fluid lag’ in models of fluid-driven fracture (e.g. Lister 1990; Garagash & Detournay 2000; Detournay 2016), is motivated by the possibility of exsolution or evaporation of gasses from the main fluid due to the low relative pressures in the peeling tip. A local travelling-wave analysis shows that the frontal speed is given by $v = (B^3 \kappa^7/p_0)^{1/2}/\mu$, where the curvature κ is again determined by matching to the interior solution.

In this paper we show that there is no need to invoke a prewetting film or precursor phase to find physical boundary conditions for propagating solutions to (1.1). Instead, we recognise that (1.1) was derived from a thin-sheet approximation to the equations of elasticity, based on the overall x and y length scales being much larger than d . This approximation breaks down within an $O(d)$ distance from any front, and in this region the full equations of elasticity should be used instead to determine the stress and deformation fields. The full equations in this region lead to a local crack-propagation problem which is driven by the bending moment applied from the interior solution and is resisted by the combined effects of the viscous flow into the crack tip and the fracture toughness of any bonding between the sheet and the substrate. We show that when viscosity is significant the rate of propagation is given by $v = B\kappa^3 d F/\mu$, where $F(k_{Ic}, k_{IIc})$ is a function of the dimensionless fracture toughnesses, k_{Ic} and k_{IIc} , which may be zero for the case of no bonding.

If the viscous pressures are not significant, as in a dry crack, the problem reduces to one in fracture mechanics, for which the propagation criterion is simply that the stress intensity at the crack tip should exceed the fracture toughness. Motivated by obvious applications to the processes of delamination and spalling, Zlatin & Khrapkov (1986), Thouless *et al.* (1987) and Suo & Hutchinson (1990) calculated the stress intensities at the tip of semi-infinite or finite cracks running parallel to the free surface of an elastic solid in terms of the remote loading. Dyskin *et al.* (2000) and Bunker & Detournay (2005) showed how Zlatin & Khrapkov's stress intensities can be used in conjunction with beam

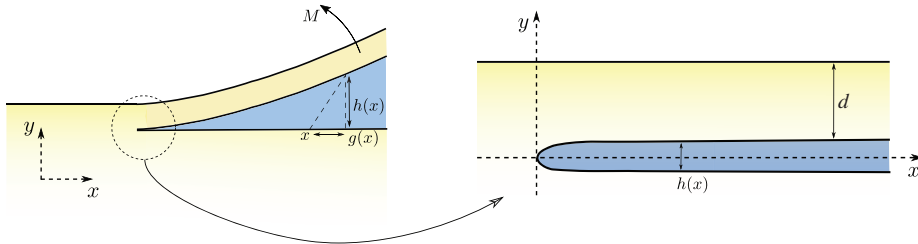


FIGURE 1. A sketch of the geometry of the problem. A bending moment M peels an elastic sheet of thickness d away from an elastic solid. The relative displacement of the sheet from the solid is g in the x direction and h in the y direction, and the gap of width h is filled with viscous fluid. On the right is a close-up of the crack tip.

or plate theory to describe toughness-controlled growth of an inviscid pressurized blister. A key result is that the loading of the crack tip is dominated by the bending moment.

Zhang *et al.* (2002, 2005) calculated solutions for fluid-driven propagation of a penny-shaped hydraulic fracture beneath a surface using the full elasticity equations for the whole problem to avoid making any assumptions about the depth-to-radius ratio. The problem considered here can be regarded as a near-tip asymptotic limit of their work, which is particularly suited to shallow viscously-controlled fracture such as the laccolith problem. Our aim is to determine simple expressions for the rate of propagation at the tip that can then be used as boundary conditions for a general interior problem without further extensive computations.

We begin in §2 by formulating a travelling-wave problem to describe propagation of a fluid-filled crack, and then describe its numerical solutions in §3. Initially, we assume that the crack propagates with fluid filling the crack tip, but discover that if the bond between the sheet and the substrate is sufficiently weak, then there must be a region of dry shear failure ahead of the fluid front. We extend the calculations to describe this situation in §4. Having obtained a full set of solutions for the propagation speed of the crack in terms of the applied bending moment, viscous resistance and toughness, we illustrate their application in §5 to determine straightforwardly the rate of spread of an axisymmetric fluid-filled blister in a number of different regimes.

2. Formulation of the problem

2.1. Physical and mathematical description

Consider a semi-infinite elastic solid, from which an elastic sheet of uniform thickness d is being peeled off on one side by application of a constant bending moment M (see figure 1). The thin gap, or crack, on the peeling side is filled with incompressible fluid of viscosity μ . (The additional effects of fluid lag could also be included in the model, but are omitted here for simplicity.)

We assume that the sheet and the solid are initially bonded together at their interface, and that the strength of the bond can be described by fracture toughnesses K_{Ic} and K_{IIc} for tensile and shear failure respectively (mode I and mode II fracture). We assume that the strength of the interface is less than the strength of either elastic solid so that the crack produced by the applied bending moment propagates along the interface. Such interfacial planes of weakness arise naturally in laminated materials, between sedimentary strata in geology and in analogue experiments (e.g. Suo & Hutchinson 1990; Pollard & Johnson 1973; Kavanagh *et al.* 2017). To reduce the number of dimensionless parameters for simplicity, we assume that the sheet has the same elastic properties as the solid, though

our calculations could easily be generalized to dissimilar materials using the techniques described in Suo & Hutchinson (1990).

We take axes as shown in figure 1, with the crack aligned along the x -axis and the crack tip instantaneously at the origin. Let $h(x)$ and $g(x)$ be the normal and tangential elastic displacements of the crack walls relative to each other. These displacements can each be represented by a distribution of dislocations along the crack, of densities $h'(x)$ and $g'(x)$ respectively, where primes denote d/dx . The dislocation densities can be shown to require opposing tractions on the crack faces given by

$$\begin{bmatrix} \sigma_{yy}(x) \\ \sigma_{xy}(x) \end{bmatrix} = -\bar{E} \int_0^\infty \mathbf{K} \left(\frac{\tilde{x} - x}{d} \right) \begin{bmatrix} h'(\tilde{x}) \\ g'(\tilde{x}) \end{bmatrix} \frac{d\tilde{x}}{d}, \quad (2.1)$$

(e.g. Head 1953; Thouless *et al.* 1987; Yang & Li 1997), where $\bar{E} = E/(1 - \nu^2)$ is the modulus for plane strain, and

$$\mathbf{K}(\xi) = -\frac{4}{\pi} \begin{bmatrix} \frac{4-3\xi^2}{\xi(\xi^2+4)^3} & \frac{3\xi^2-4}{2(\xi^2+4)^3} \\ \frac{4-3\xi^2}{2(\xi^2+4)^3} & \frac{\xi^4+\xi^2+4}{\xi(\xi^2+4)^3} \end{bmatrix}. \quad (2.2)$$

For the fluid-loaded crack of interest here, we have $\sigma_{yy} = -p$, where $p(x)$ is the fluid pressure, and $\sigma_{xy} = 0$. (The viscous shear stresses due to flow have the wrong symmetry to contribute to the relative displacements, and are also much smaller than the fluid pressures.) Thus (2.1) can be regarded as an integral equation relating the crack shape to the fluid pressure.

We use lubrication theory to describe the viscous flow in the thin gap. Hence the fluid pressure gradients drive a flux

$$q = -\frac{h^3}{12\mu} \frac{dp}{dx}. \quad (2.3)$$

We look for a travelling-wave solution of the form $h(x + vt)$, propagating leftwards with constant speed v . For such a solution, we deduce from mass conservation that $q = -vh$ and hence

$$\frac{dp}{dx} = \frac{12\mu v}{h^2}. \quad (2.4)$$

The coupled equations (2.4) and (2.1) require boundary conditions for propagation at the crack tip and for prescribing the applied bending moment.

The stress intensities K_I and K_{II} at the crack tip can be determined from the asymptotic behaviour (Rice 1968)

$$h(x) \sim \frac{K_I}{\bar{E}} \left(\frac{32x}{\pi} \right)^{1/2}, \quad g(x) \sim \frac{K_{II}}{\bar{E}} \left(\frac{32x}{\pi} \right)^{1/2} \quad \text{as } x \rightarrow 0_+ \quad (2.5)$$

of the displacements near the tip. Assuming linear elastic fracture mechanics, the condition for crack propagation is that the stress intensity is equal to the fracture toughness (Kanninen & Popelar 1985). We assume for now that the crack is propagating as a simple mode-I (tensile) fracture, which requires $K_I = K_{Ic}$.

For $x \gg d$, the displacement of the sheet can be described asymptotically by beam theory (Dyskin *et al.* 2000), which gives

$$p(x) = \frac{\bar{E}d^3}{12} h'''' \quad \text{and} \quad m(x) = \frac{\bar{E}d^3}{12} h'', \quad (2.6)$$

where $m(x)$ is the local bending moment. We are considering peeling driven by an applied remote bending moment M , and so $m(x) \rightarrow M$ as $x \rightarrow \infty$, which gives a boundary

condition on h'' . Hence the gap h between the sheet and the solid widens rapidly to the right like x^2 and, from (2.4), the pressure gradient decreases rapidly like x^{-4} , confirming that the viscous resistance is dominated by the $O(d)$ neighbourhood of the tip. Since we are considering peeling-by-bending here rather than peeling-by-pulling (Lister *et al.* 2013), we assume that there isn't any remote tension also being applied to the sheet (or that it is much smaller than M/d and thus negligible). Nevertheless, the upward curvature h'' of the sheet implies that its lower surface is in extension with strain $dh''/2$ (and its upper surface is in compression with strain $-dh''/2$). The remote loading conditions are thus equivalent to

$$\frac{\bar{E}d^3}{12}h'' \sim M, \quad g' \sim \frac{d}{2}h'' \quad \text{as} \quad x \rightarrow \infty \quad (2.7a, b)$$

2.2. Nondimensionalization

We define dimensionless variables as follows:

$$x = d\xi, \quad h(x) = \frac{M}{\bar{E}d}H(\xi), \quad g(x) = \frac{M}{\bar{E}d}G(\xi), \quad (2.8)$$

$$p = \frac{M}{d^2}P(\xi), \quad K_I = Md^{-3/2}k_I, \quad K_{II} = Md^{-3/2}k_{II}, \quad V = \frac{\mu\bar{E}^2d^5v}{M^3}. \quad (2.9)$$

With these scalings, the equations become

$$\begin{bmatrix} P \\ 0 \end{bmatrix} = \int_0^\infty \mathbf{K}(\tilde{\xi} - \xi) \begin{bmatrix} H'(\tilde{\xi}) \\ G'(\tilde{\xi}) \end{bmatrix} d\tilde{\xi} \quad (2.10)$$

$$H^2P' = 12V \quad \text{or} \quad P(\xi) = -12V \int_\xi^\infty \frac{d\tilde{\xi}}{H(\tilde{\xi})^2} \quad (2.11a, b)$$

$$\lim_{\xi \rightarrow \infty} H'' = 12, \quad \lim_{\xi \rightarrow \infty} G' = 6 \quad (2.12)$$

$$k_I = \chi \lim_{\xi \rightarrow 0} \sqrt{\xi}H', \quad k_{II} = \chi \lim_{\xi \rightarrow 0} \sqrt{\xi}G', \quad (2.13)$$

where $\chi = (\pi/8)^{1/2}$. (We chose not to absorb χ into our definitions of k_I and k_{II} in order to maintain consistency with Zlatin & Khrapkov (1986) and Thouless *et al.* (1987); Detournay and co-workers define $K'_{ic} = 2K_{ic}/\chi$.)

2.3. Numerical solution

It was found convenient to solve (2.10)–(2.12) numerically for a given value of V , and then infer the corresponding values of $k_I(V)$ and $k_{II}(V)$ from (2.13). The first of these relationships could then be inverted, with $k_I = k_{Ic}$, to give the speed V in terms of the toughness k_{Ic} , which is the natural physical interpretation.

We discretized the equations by taking $n+1$ points $\xi_0 = 0 < \xi_1 < \dots < \xi_n$ at which to represent H' and G' . Typically, $n \approx 500$ and $\xi_n \approx 800$. The choice of points and of the interpolation of H' and G' between the points both took account of the square-root singularities at the tip. (The details are described in appendix A.) Given the $2(n+1)$ coefficients of the interpolating functions, the integrals in (2.10) and (2.11b) can all be done analytically. We obtain n equations from equating the two expressions for P at n midpoints $\xi_{i+1/2} \in [\xi_i, \xi_{i+1}]$, n equations from the condition $\sigma_{xy} = 0$ at those midpoints, and two equations from the limiting behaviour (2.12). This system of equations was solved by Newton's method.

In order to apply the limits (2.12) to the information in $\xi \leq \xi_n$, we develop an

asymptotic expansion using the beam approximation (2.6) for $\xi \gg 1$. In the dimensionless variables, $P = H''''/12$, which we combine with (2.11a) to obtain

$$H'''' = 144V/H^2. \quad (2.14)$$

But we know from (2.12) that $H(\xi) = 6\xi^2 + o(\xi^2)$, as $\xi \rightarrow \infty$, and so we can solve (2.14) iteratively to find

$$\frac{1}{12}H''(\xi) = 1 - \frac{V}{18\xi} - \frac{V^2}{18^2} \frac{\ln \xi}{\xi^2} + O(1/\xi^2), \quad \text{and} \quad G' = H''/2 \quad (2.15)$$

from (2.7b). These conditions can be used at ξ_n in place of (2.12). (The $O(1/\xi^2)$ correction in (2.15) cannot be determined solely from the far-field behaviour.)

3. Results

For $V = 0$ the problem is static, there are no viscous pressures and (2.10)–(2.12) simply describe a semi-infinite crack beneath a free surface that is loaded by a remote bending moment. This problem was solved by Zlatin & Khrapkov (1986), who found that $(k_I, k_{II}) = (1.932, 1.506)$, which agrees with, and provides a check on, our numerical results.

Using the case $V = 0$ as a starting solution, we increased V , iterated the Newton scheme to convergence, and then repeated to obtain a sequence of solutions for increasing values of V . Two typical results for H' , G' , and P with $V = 0.1$ and 0.65 are shown in figure 2, along with the expected asymptotic behaviour for $\xi \ll 1$ and $\xi \gg 1$. (The behaviour of P follows from $P' = 12V/H^2$ and the behaviour of H .) We note that the larger value of V requires a larger negative pressure in $\xi \ll 1$ to suck fluid into the opening gap; the larger negative pressure in the tip reduces the values of H' by pulling the crack walls together. In particular, it reduces the stress intensity $k_I = \chi \lim_{\xi \rightarrow 0} \xi^{1/2} H'(\xi)$. Alternatively put, some of the applied remote bending moment is supported by the negative fluid pressures, so that less stress is applied to the tip.

The variation of k_I with V is shown in figure 3, confirming a monotonic decrease of k_I as the viscous pressure drop in the tip increases. It is perhaps not surprising that as $k_I \rightarrow 0$ (negligible toughness) the speed V tends to a finite limit $V_0 \approx 0.678$ determined entirely by the fluid-mechanical resistance to propagation. It is initially more surprising that the approach to this limit is singular, with k_I behaving locally like $(V_0 - V)^{0.316}$.

Some insight can be obtained by considering the behaviour of H' near the tip as $V \rightarrow V_0$ (or $k_I \rightarrow 0$), as shown in figure 4. While $H' \sim (k_I/\chi)\xi^{-1/2}$ as $\xi \rightarrow 0$, as $k_I \rightarrow 0$ more and more of the near-tip solution looks like $H' \sim A\xi^{-1/3} + O(\xi^{-4/3})$ for $A \approx 4.2$, with the $k_I\xi^{-1/2}$ behaviour confined to a boundary layer near $\xi = 0$. This sort of boundary-layer structure was discovered and analysed by Garagash & Detournay (2005) in the context of finite or semi-infinite cracks propagating through an infinite elastic solid with a small dimensionless fracture toughness. We can establish the connection as follows.

For a fluid-driven crack with $k_I = 0$ it should be anticipated that the crack-tip opening and pressure are governed by a viscous–elastic balance with $H \propto \xi^{2/3}$ and $P \propto \xi^{-1/3}$ as $\xi \rightarrow 0$ (Spence & Sharp 1985; Lister 1990; Desroches *et al.* 1994). Crucially, this balance is locally determined in the tip, and is independent of more-remote loading or boundary conditions. For $\xi \ll 1$, the elasticity kernel (2.2) and integral (2.10) reduce to the much simplified form

$$P(\xi) = \frac{1}{4\pi} \int_0^\infty \frac{H'(\tilde{\xi})}{\tilde{\xi} - \xi} d\tilde{\xi}, \quad (3.1)$$

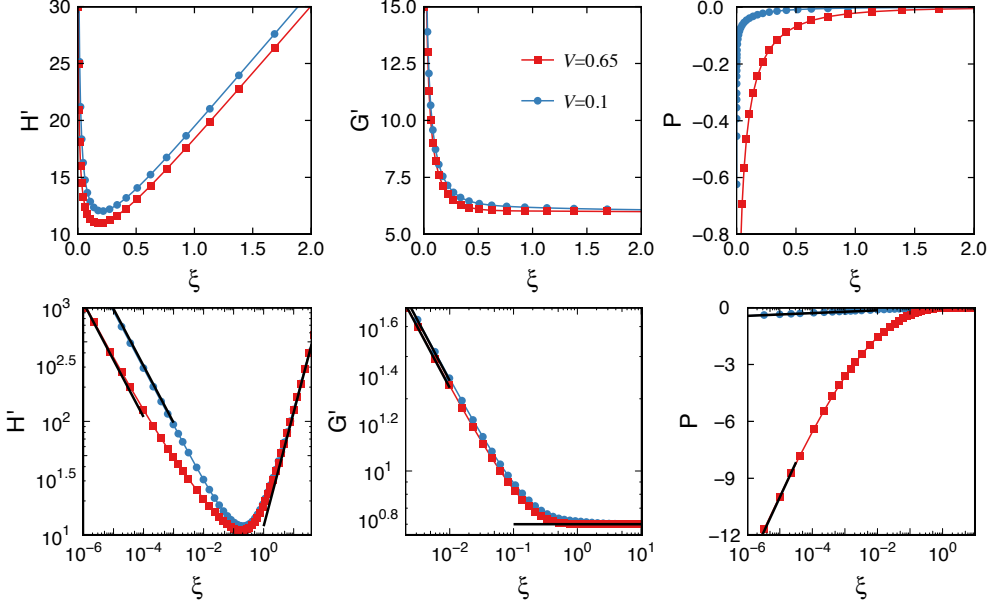


FIGURE 2. Numerical solutions for the dislocation densities H' and G' and the pressure P for speeds $V = 0.1$ and 0.65 (stress intensities $k_I = 1.83$ and 0.69). The second row of figures uses logarithmic scales to show the expected asymptotic behaviour (solid lines): $H' \sim (k_I/\chi)\xi^{-1/2}$, $G' \sim (k_{II}/\chi)\xi^{-1/2}$, $P \sim (3\chi^2 V/k_I^2) \ln \xi$ as $\xi \rightarrow 0$, where $\chi = (\pi/8)^{1/2}$; and $H' \sim 12\xi$, $G' \rightarrow 6$, $P \rightarrow 0$ as $\xi \rightarrow \infty$.

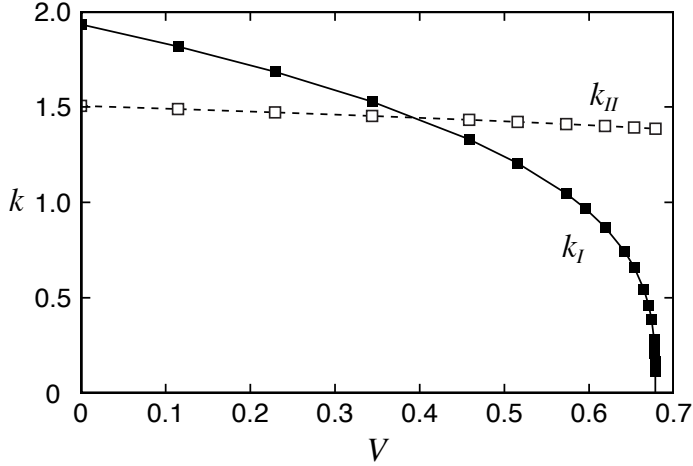


FIGURE 3. The mode-I stress intensity k_I as a function of the speed V (filled symbols). Also shown for discussion in §4 is the mode-II stress intensity k_{II} (open symbols).

which is the same as that for a semi-infinite crack in an infinite solid. For the case $k_I = 0$, (3.1) and (2.11) have leading-order solutions

$$H_0 = 6(3V_0^2)^{1/6}\xi^{2/3} + o(\xi^{2/3}), \quad P_0 = -\left(\frac{V_0}{3\xi}\right)^{1/3} + o(\xi^{-1/3}) \quad (3.2)$$

With $V_0 = 0.678$, (3.2) gives $H' \sim 4.22\xi^{-1/3}$ in agreement with figure 4.

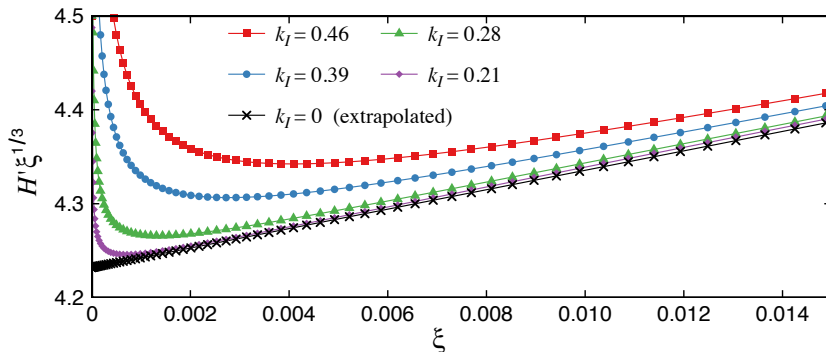


FIGURE 4. The near-tip behaviour of H' as k_I decreases towards 0. The $\xi^{-1/2}$ behaviour is increasingly confined to a very thin region near $\xi = 0$, while more and more of the solution tends towards $H' \sim \xi^{-1/3}$. We did not calculate H' directly for $k_I = 0$, but show an extrapolation to it.

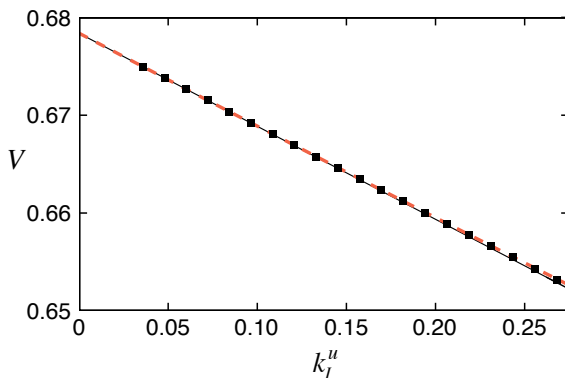


FIGURE 5. The numerical values of k_I^u are plotted as points against the values of V . A linear fit from the two smallest k_I values is plotted as a solid line, a quadratic fit from the three smallest k_I values is plotted as a dashed line. They are almost indistinguishable at this scale. The difference between the two fits at $k_I = 0$ is only $\approx 0.002\%$, which provides an estimate of the error in extrapolating to calculate V_0 (not accounting for the discretization error due to n).

However, for $k_I > 0$ (3.2) does not satisfy the tip condition (2.13). Garagash & Detournay (2005) showed how (2.13) can be satisfied for $0 < k_I \ll 1$ by introducing a so-called ‘LEFM’ boundary-layer on the small scale $\xi = O(k_I^6)$, where $H = O(k_I^4)$, and matching this inner solution to (3.2) as the leading-order outer solution. They also found that the boundary-layer leads to $O(k_I^{4-6s})$ corrections to the outer solution, where $s \approx 0.139$ comes from solving a transcendental equation and $u \equiv 4 - 6s \approx 3.168$. In appendix B, we show how this correction term can be used to calculate an asymptotic prediction $V \approx V_0 - 0.0950k_I^u$ as $k_I \rightarrow 0$. Figure 5 shows that there is remarkably good agreement with this linear prediction, even for relatively large values of k_I .

4. Dry cracking ahead of the fluid front

Thus far, we have been assuming for simplicity that the crack propagates as a simple mode-I (tensile) fracture, with speed V determined by the dimensionless criterion $k_I(V) = k_{Ic}$ for tensile failure. However, owing to the asymmetry of the geometry about $y = 0$, both the remote bending moment and the fluid-pressure loading result in some

mode-II (shear) loading of the crack tip and not just in tensile loading. The failure criterion for such mixed-mode loading of an interfacial crack is found experimentally to be fairly well represented by the elliptical form

$$k_I^2 + \lambda k_{II}^2 = k_{Ic}^2, \quad (4.1)$$

where k_I and k_{II} are the stress intensities (2.13) at the tip, $\lambda^{1/2} = K_{Ic}/K_{IIc} = k_{Ic}/k_{IIc}$ is the ratio of the fracture toughnesses for pure tensile loading and pure shear loading, and λ is typically 0.1–0.2 (Jensen *et al.* 1990; Yuuki *et al.* 1994).

As V increases from 0 to the limiting speed 0.678 for the solutions calculated in §3, k_I decreases monotonically from the static value 1.932 (Zlatin & Khrapkov 1986) down to 0 (see figure 3), and k_{II} decreases slowly and monotonically from the static value 1.506 to about 1.385. Provided $1.385^2\lambda < k_{Ic}^2 < 1.932^2 + 1.506^2\lambda$, there is thus a unique value of V and solution from §3 that satisfies the failure criterion (4.1). However, if $k_{IIc} = k_{Ic}\lambda^{-1/2} < 1.385$ even the fastest solution from §3 has $k_{II} > k_{IIc}$ (and $k_I = 0$); the crack tip is under greater shear stress than it can withstand, and we would expect the crack to propagate faster as a result. We infer that shear failure at the crack tip must allow it to outrun the fluid front, such that there is a region of dry shear between the crack tip and the fluid front. (This phenomenon should be distinguished from the concept of ‘fluid lag’, which is caused by vapour in a low-pressure tip rather than dry shear failure.) We now analyse this possibility.

4.1. Equations

Suppose the crack tip is at $\xi = -L$ and the fluid front is at $\xi = 0$ in the frame of a travelling-wave solution propagating to the left. Along the dry part of the crack, $-L < \xi < 0$, the crack walls are in contact and so the normal displacement is zero, $H(\xi) = H'(\xi) = 0$. We assume here, for simplicity, that friction on the crack walls is negligible and so the tangential displacement $G(\xi)$ is such that the shear stress is zero, $\sigma_{xy} = 0$. (Future work might explore the effects of different friction laws.) The elastic equation (2.10) is thus unaltered except for replacing the lower limit in the integral by $-L$. The lubrication equation (2.11) and far-field conditions (2.12) are likewise unaltered.

Now let

$$k_I \equiv \chi \lim_{\xi \rightarrow -L} \sqrt{\xi + L} H'(\xi), \quad k_{II} \equiv \chi \lim_{\xi \rightarrow -L} \sqrt{\xi + L} G'(\xi), \quad k_I^f \equiv \chi \lim_{\xi \rightarrow 0} \sqrt{\xi} H'(\xi), \quad (4.2)$$

where $\chi = (\pi/8)^{1/2}$, so that k_I and k_{II} denote the usual stress intensities for a crack tip at $\xi = -L$. Here $H' = 0$ in the dry part $\xi < 0$, and so $k_I = 0$ follows automatically. The criterion for crack-tip propagation at $\xi = -L$ is thus $k_{II} = k_{IIc}$ corresponding to simple shear failure. The third stress intensity k_I^f denotes the strength of the singularity at $\xi = 0$ that would, in general, result from solving the elastic problem with $P(\xi)$ prescribed in $\xi > 0$ and $H = 0$ prescribed in $\xi < 0$. Here, however, the solid had already fractured at $\xi = 0$ and has no strength to support a nonzero stress intensity. Hence the location and speed of the fluid front must be such that $k_I^f = 0$.

The physical boundary conditions at the fluid front and the crack tip are thus $k_I^f = 0$ and $k_{II} = k_{IIc}$, and these two conditions determine the dry length L and speed V of the solution. In practice, it is more convenient numerically to prescribe values of L and V , solve for the geometry to find the values of $k_I^f(V, L)$ and $k_{II}(V, L)$, and then invert the first relationship to impose the physical condition $k_I^f = 0$. Further details are given in appendix A.3.

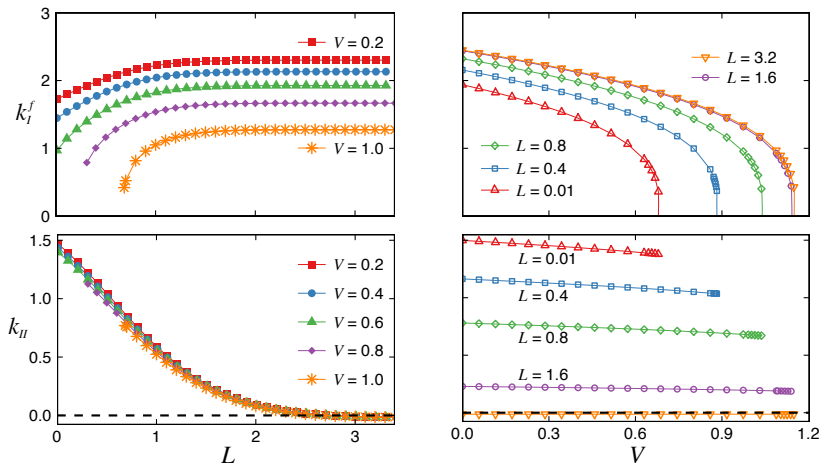


FIGURE 6. Values of the stress intensities k_I^f at $\xi = 0$ and k_{II} at $\xi = -L$ as functions of the dry crack length L ahead of the fluid front and the speed V of propagation. The desired physical solutions are those with $k_I^f = 0$, which then implies a relationship between L and V .

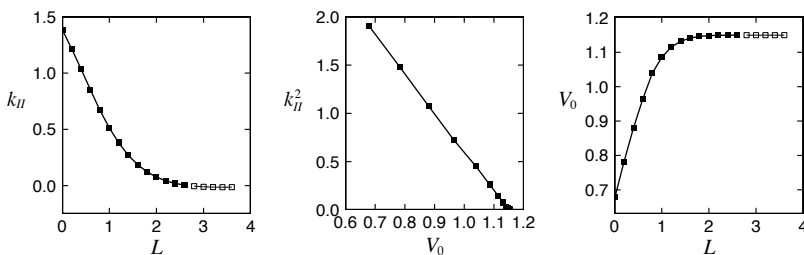


FIGURE 7. The relationships between speed V_0 , dry length L and stress intensity k_{II} for solutions with $k_I^f = 0$. These give a unique solution with $k_I^f = 0$ and $k_{II} = k_{IIc}$ for $0 \leq k_{IIc} \leq 1.385$. Negative values of $k_{II} < 0$ (hollow squares) do not correspond to a physically attainable solution.

4.2. Results

In figure 6 we show the values of k_I^f and k_{II} for varying L at fixed V and for varying V at fixed L . The most significant observations are: (i) Increasing the length L of the dry region relieves the shear loading of the crack tip; the stress intensity k_{II} decreases monotonically from the values 1.506–1.385 obtained for $L = 0$ down to zero for $L \approx 2.7$, and we can thus find solutions with $k_{II} = k_{IIc}$. (ii) Increasing the speed V decreases the (unphysical) tensile stress intensity k_I^f at the fluid front, with k_I^f approaching zero (the desired value for an already-fractured solid) in the same power-law way as seen previously in figure 3 and analysed in appendix B.

For fixed L we extrapolate these results to find where $k_I^f = 0$ at some speed $V_0(L)$ with a corresponding stress intensity $k_{II}(L)$. The relationships between V_0 , L and k_{II} corresponding to the solutions with $k_I^f = 0$ are shown in figure 7. As hoped, we obtain a unique solution $k_{II} = k_{IIc}$ for each value of k_{IIc} in the range 0–1.385 not covered by the solutions of §3. As might be expected, both L and V_0 increase as the toughness of the solid decreases, and reach finite limits as $k_{IIc} \rightarrow 0$. (The solutions with $k_{II} < 0$ for $L \gtrsim 2.7$ are not physically attainable since they do not correspond to a stable equilibria, nor can they be reached by the tip extending from zero.) The relationship between V_0 and k_{II}^2 is approximately linear with $V_0 \rightarrow 1.15$ as $k_{II} \rightarrow 0$.

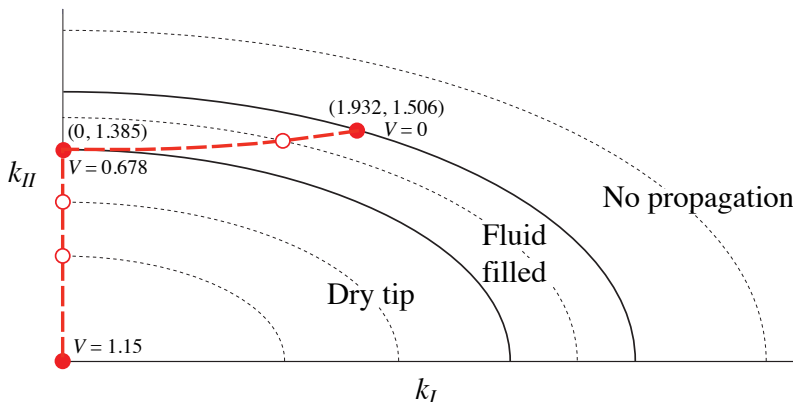


FIGURE 8. The failure criterion (4.1) for mixed-mode loading of the crack tip defines an ellipse $(k_I/k_{Ic})^2 + (k_{II}/k_{IIc})^2 = 1$ with semi-axes of lengths $k_{ic} = K_{ic}d^{3/2}/M$. For large K_{ic} (small M) the ellipse does not intersect either solution curve (dashed) and there is no propagation; for smaller K_{ic} (larger M) the ellipse intersects one of the two solution curves (circles) and the crack propagates either with a fluid-filled tip or with a preceding dry shear crack. The dimensionless speed V depends on the point of intersection.

5. Summary and application to blisters

5.1. Summary of regimes

The results of §§3 and 4 allow us to find solutions for all values of the dimensionless fracture toughnesses k_{Ic} and k_{IIc} (see figure 5.1). First, from (4.1) and the static values of k_I and k_{II} (Zlatin & Khrapkov 1986), we deduce that if $(1.932/k_{Ic})^2 + (1.506/k_{IIc})^2 < 1$ then the material is too tough and the crack will not propagate. Secondly, if $k_{IIc} < 1.385$ then the material is sufficiently weak that the crack will propagate as described in §4 with a dry shear crack of length $L(k_{IIc})$ preceding the fluid front, and with the speed set by the condition $k_{II}(V) = k_{IIc}$. Thirdly, if k_{Ic} and k_{IIc} lie between the first and second regimes then the crack will propagate as described in §3 with fluid filling the crack tip, and with the speed set by the condition that $k_I(V)$ and $k_{II}(V)$ satisfy (4.1). Recall that fluid lag was assumed negligible for simplicity, but could be included in future work. (While we have assumed a failure criterion of the form (4.1), the method could easily be generalized to any sensible criterion of the form $G(k_I, k_{II}) = G_c$.)

Our calculations thus provide the dimensionless propagation speed V of the crack as a function of the remote loading, viscous resistance and fracture toughness. These solutions are near-tip asymptotics which describe the peeling process at the front of a larger-scale problem that provides the remote bending stress. In order to facilitate use of our results as an effective boundary condition for the larger-scale problem, without having to repeat all the numerical computations, we provide the following empirical fits for the relationships between speed and stress intensity from §§3 and 4:

$$V = 0.678 - 0.095k_I^u + 0.0038k_I^{3u/2} \quad (\text{fluid-filled tip}) \quad (5.1a)$$

$$V = 0.0377 + 7.0(1.5 - k_{II}) - 12.3(1.5 - k_{II})^2 \quad (\text{fluid-filled tip}) \quad (5.1b)$$

$$V = 1.15 - 0.248k_{IIc}^2 \quad (\text{dry tip}). \quad (5.1c)$$

These equations provide very good approximations to the data, as shown in figure 9. The

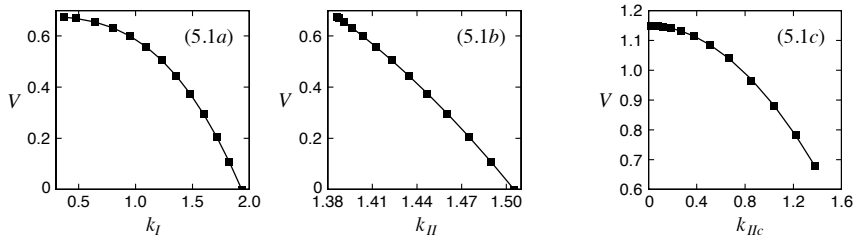


FIGURE 9. The empirical fits (5.1) (solid lines) are good approximations to the numerical solutions (symbols), allowing use as effective boundary conditions.

dimensional speed v resulting from the bending moment M is obtained from

$$v = \frac{M^3 V(k_{Ic}, k_{IIc})}{\mu \bar{E}^2 d^5}, \quad \text{where} \quad k_{Ic} = \frac{K_{Ic} d^{3/2}}{M}, \quad k_{IIc} = \frac{K_{IIc} d^{3/2}}{M}. \quad (5.2)$$

Alternatively, we can write (5.2) in terms of the bending stiffness $B = \bar{E}d^3/12$ of the sheet and the curvature $\kappa = M/B$ behind the propagating front:

$$v = \frac{Bd}{144\mu} \kappa^3 V. \quad (5.3)$$

To illustrate how these equations can be used as boundary conditions of an interior problem, we reconsider some of the axisymmetric blister problems described in Lister *et al.* (2013), but with the propagation rate determined by viscous-controlled fracture rather than by peeling from a pre-wetting film.

5.2. Application to axisymmetric propagation of blisters

Suppose an axisymmetric fluid blister of radius $R(t)$ and thickness $h(r, t)$ is formed by injecting a volumetric flux Q of fluid at $r = 0$ below an elastic sheet of thickness $d \ll R$ resting on an elastic solid. If $h \ll d$ then we can neglect stretching of the sheet above the blister, and the fluid pressure far from the edge ($R - r \gg d$) is given by the combination $p = B\nabla^4 h + \rho g(h - z)$ of bending stresses and hydrostatic pressure. As noted in the introduction, because the sixth-order equation (1.1) (and its generalization to include gravity) does not support solutions with a propagating front, we expect an interior solution where $\nabla p = \mathbf{0}$ at leading order, which must be matched to a propagating frontal solution.

Solution of $p = \text{const.}$, with $h(R) = h'(R) = 0$ yields

$$h(r) = h(0) \frac{f(R) - f(r)}{f(R) - f(0)}, \quad \text{where} \quad f(r) = \text{Im} \frac{\ell_g I_0(\omega r / \ell_g)}{\omega I_1(\omega R / \ell_g)}, \quad \omega = e^{i\pi/4}, \quad (5.4)$$

$I_0(z)$ and $I_1(z)$ are modified Bessel functions, and $\ell_g = (B/\rho g)^{1/4}$ is the ‘elastogravity’ length scale at which bending stresses and gravity have comparable effects. The variation of these shapes with R/ℓ_g is shown in figure 10. From the general solution (5.4) one can readily obtain expressions for the volume Qt and frontal curvature $\kappa = h''(R)$ and then use (5.3) to solve numerically for $R(t)$. However, it is more illuminating to consider the limits $R \ll \ell_g$ and $R \gg \ell_g$.

For $R \ll \ell_g$ bending stresses dominate the effects of gravity, and (5.4) can be simplified to

$$h(r, t) = \frac{3Qt}{\pi R^2(t)} \left(1 - \frac{r^2}{R^2(t)} \right)^2. \quad (5.5)$$

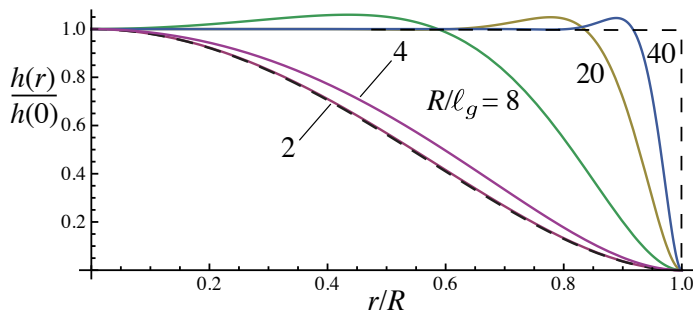


FIGURE 10. The quasistatic interior solution (5.4) for the shape of a blister of radius R for various values of R/ℓ_g (solid lines), where $\ell_g = (B/\rho g)^{1/4}$ is the elastogravity length, with the asymptotes as $R/\ell_g \rightarrow 0, \infty$ (dashed).

Assuming that the toughness of any bonding between the sheet and the solid is negligible, such that $k_{Ic} = k_{IIc} = 0$, we obtain dR/dt from (5.3) with $V = 1.15$ and $\kappa = 24Qt/\pi R^4$. Integration yields

$$R(t) = 1.21 \left(\frac{BdQ^3}{\mu} \right)^{1/13} t^{4/13}, \quad (5.6)$$

$$h(0, t) = 0.66 \left(\frac{\mu Q^7}{Bd} \right)^{1/13} t^{5/13}. \quad (5.7)$$

For $R \gg \ell_g$ the effects of gravity dominate and the blister is flat-topped (like a large-Bond-number puddle) except within $O(\ell_g)$ of the edge where the bending stresses result in a peripheral shape

$$h = \frac{Qt}{\pi R^2} \left(1 - \text{Im} \frac{\exp[\omega(R-r)/\ell_g]}{\omega} \right) \quad (5.8)$$

with frontal curvature $\kappa = Qt/\pi R^2 \ell_g^2$. Again assuming negligible toughness and purely viscous control such that $V = 1.15$, we integrate to obtain

$$R(t) = 0.33 \left(\frac{BdQ^3}{\mu \ell_g^6} \right)^{1/7} t^{4/7}, \quad (5.9)$$

$$h(0, t) = 2.88 \left(\frac{\mu Q \ell_g^6}{Bd} \right)^{1/7} t^{-1/7}. \quad (5.10)$$

From (5.6)–(5.7) we find that $M \propto h''(R) \propto t^{-3/13}$ for $R \ll \ell_g$ and from (5.9)–(5.10) that $M \propto t^{-1/7}$ for $R \gg \ell_g$. It follows that if the toughness is not actually zero then from (5.2) k_{Ic} and k_{IIc} will increase with time, and the effects of toughness will eventually become significant. The resultant transition period toward toughness control has no analytical solution, but requires numerical solution using (5.5) or (5.8) to relate $M = B\kappa$ to the radius R , and then (5.2) to find dR/dt . The numerical problem is only an ordinary differential equation coupled to a few algebraic equations, and is easily programmed.

The long-term limit beyond this transition period is controlled by toughness rather than viscosity. In the toughness regime R increases with volume Qt in such a way that a quasistatic equilibrium is maintained, wherein the static stress intensities due to M (Zlatin & Khrapkov 1986) lie on the yield criterion (4.1). Thus M is given by the static

yield criterion

$$M = d^{3/2}[(1.932/K_{Ic})^2 + (1.506/K_{IIc})^2]^{-1/2}, \quad (5.11)$$

and both M and $\kappa = M/B$ are constant. Using (5.5) or (5.8), we find that

$$R \propto \left(\frac{BQt}{K_{Ic}d^{3/2}} \right)^{1/4} \quad (R \ll \ell_g) \quad \text{or} \quad R \propto \left(\frac{BQt}{\ell_g^2 K_{Ic}d^{3/2}} \right)^{1/2} \quad (R \gg \ell_g) \quad (5.12)$$

in agreement with detailed calculations by Bunker & Detournay (2005) and Bunker & Cruden (2011).

A transition of a different kind occurs if h in (5.7) increases to $O(d)$. In this case the tension due to stretching of the sheet above the blister can no longer be neglected and one should instead calculate the shape of the blister using the Föppl-von Karman equations (see Jensen 1991; Lister *et al.* 2013). As h/d increases, this modifies the relationship giving the peripheral bending moment M in terms of the volume Qt and radius R . Moreover, it is found that the radial tension T increases to $O(M/d)$ from $O(Mh/d^2)$ and so starts to contribute at leading order to the effective far-field loading of the near-tip problem. In particular, (2.12) needs to be modified to $G' \rightarrow 6 + Td/M$ as $\xi \rightarrow \infty$, where the value of Td/M is determined by the interior blister solution. While this introduces another dimensionless parameter Td/M to the near-tip problem, and thus affects the numerical value of the dimensionless speed V , it does not change the dimensional scaling of the speed v in (5.2).

For $d \ll h \ll R \ll \ell_g$, the interior solution can be found by neglecting bending stresses and solving the membrane equations to obtain a roughly parabolic shape that approaches $r = R$ with a slope $\theta \propto Qt/R^3$ and tension $T \propto \bar{E}d(Qt/R^3)^2$ (see Lister *et al.* 2013) (This is the elastic analogue to the spherical-cap shape of a capillary drop with small contact angle.) This peripheral slope is matched to a static bending boundary layer where bending stresses re-enter the problem to give

$$h' = \theta \{e^{(r-R)(T/B)^{1/2}} - 1\}. \quad (5.13)$$

The bending boundary-layer width, $(B/T)^{1/2} = O(d/\theta)$, is much larger than the $O(d)$ length scale of the near-tip viscous solution. The near-tip solution is thus nested within the boundary layer and forced by a bending moment $M = \frac{1}{12}(BT)^{1/2}\theta \propto (B/d)(Qt/R^3)^2$ and by the tension $T \propto \bar{E}d(Qt/R^3)^2$. (The ratio Td/M is a constant for $h \gg d$.) We substitute the scale of the bending moment into the dimensional scaling of (5.2) and integrate to obtain

$$R \propto \left(\frac{\bar{E}dQ^6}{\mu} \right)^{1/19} t^{7/19}. \quad (5.14)$$

Again M decreases, like $t^{-6/19}$, and there would be an eventual transition to toughness control.

5.3. Comparison with other spreading mechanisms

The examples given in the previous subsection show how straightforwardly to apply the propagation speed (5.2) as a boundary condition to determine growth by fracture of a fluid-driven blister in three different forcing regimes, in which the interior shape is dominated by bending stresses, gravity or tension respectively. In each case there is a transition from viscous control to toughness control for fixed-flux injection. These solutions are also easy to generalize to the case where the volume of fluid is of the form Qt^α , for some α , perhaps due to fixed-pressure or fixed-volume injection.

	Bending	Gravity	Tension
Viscous-controlled tip	$(3\alpha + 1)/13$	$(3\alpha + 1)/17$	$(6\alpha + 1)/19$
Toughness-controlled tip	$\alpha/4$	$\alpha/2$	$\alpha/3$
Prewetting film	$(5\alpha + 2)/22$	$(5\alpha + 2)/12$	$(5\alpha + 1)/16^\dagger$
Vapour-filled tip	$(7\alpha + 2)/30$	$(5\alpha + 2)/16$	$(7\alpha + 1)/22^\dagger$

TABLE 1. Spreading exponents β in $R \propto t^\beta$ for the axisymmetric spread of a blister of volume Qt^α , in regimes driven by bending stresses, gravity or tension in the interior, and resisted by different mechanisms at the tip.

[†] Assuming the dominant viscous resistance is nested inside the bending boundary layer (5.13).

The same three forcing regimes were analysed by Lister *et al.* (2013) in the context of a blister that spreads by peeling of an elastic sheet away from a pre-wetting film of fluid between the sheet and the substrate. The interior solutions were the same, but the peeling process results in a propagation speed $v \propto (B^2 h_0 \kappa^5)^{1/2} / \mu$ rather than (5.2).

Hewitt *et al.* (2015) analysed the three regimes in the context of a two-dimensional blister that can spread because a low-viscosity precursor phase at a fixed pressure $-p_0$ occupies the propagating front. If the extent of this fluid lag is much greater than $O(d)$ then one can use beam theory to calculate a frontal speed $v \propto (B^3 \kappa^7 / p_0)^{1/2} / \mu$. This has recently been confirmed in axisymmetric experiments by Ball & Neufeld (2018) and extended to include toughness by Wang & Detournay (2018). If the extent of the fluid lag is $O(d)$, or less, then one should instead generalize the elastohydrodynamic description in §2 to replace the lubrication equation (2.11) by $P = -P_0$ in some lag region $0 < \xi < \xi_0$. In the context of hydraulic or magma fracture the large confining pressure means the lag length is very unlikely to be much greater than the thickness d of the overburden, and thus the generalized elastohydrodynamic description seems a more appropriate way to address lag in these cases than beam theory.

In table 1 we show the various spreading exponents for the three forcing regimes and the four spreading control mechanisms for the general case of fluid volume proportional to t^α . The exponents for each regime are quite similar in numerical value for $\alpha = 1$ despite the different mechanisms. This table is actually far from exhaustive when considering the range of possible peeling regimes, and a fuller categorization is given by Peng (2017). We note that the exponents for toughness control are the same as those for simpler models with a prescribed interfacial energy of adhesion or with capillary adhesion (Peng 2017; Ball & Neufeld 2018).

6. Conclusions

The peeling by fluid injection of an elastic sheet away from a substrate is often regularized by invoking a thin prewetting film or a low-viscosity phase in the tip. In this paper, we have instead analysed fluid-driven peeling without such precursors, by considering an elastic sheet either bonded to, or simply laid on, an elastic substrate. To resolve the ‘elastic contact-line problem’ that arises from a naive combination of lubrication theory and beam theory, we recognized that the beam approximation breaks down near the propagating tip, and instead the full equations of elasticity and fracture should be combined with lubrication theory to determine the coupled pressures and deformations in this region.

We have solved numerically the resultant local crack-propagation problem, which is driven by the bending moment M applied from the interior solution and resisted by the

combined effects of viscous flow into the crack tip and the toughness of any bonding between sheet and substrate. This problem yielded a one-parameter family of solutions: for strong bonding and small bending moment, the load is supported (quasi-) statically by the toughness, and propagation is slow; for weak bonding and large bending moment, the load is supported instead by the flow-induced viscous pressure-drop in the crack tip, and the propagation rate is determined by the local elastohydrodynamics. The singular asymptotic approach (figure 5) to a finite propagation rate for the case of no bonding is given in appendix B.

Between the two limiting regimes, our calculations provide simple expressions (5.1) and (5.2) to determine the dimensionless tip propagation speed V , which can then be used as effective boundary conditions for an interior problem without further extensive computations. The dimensional speed scales like $M^3/\mu\bar{E}^2d^5 = Bd\kappa^3/144\mu$, where d is the sheet's thickness, $B = \bar{E}d^3/12$ its stiffness, $\bar{E} = E/(1 - \nu^2)$ its plane-strain modulus, and κ the limiting curvature at the edge of the interior solution. The expressions for the propagation speed have been used to derive new similarity solutions for the spread of a fluid-filled blister in a variety of different regimes (see table 1).

A geological application of these results is to the propagation and growth of laccoliths, which are large tabular near-surface magmatic intrusions that propagate along subsurface bedding planes rather than breaching the surface (Michaut 2011; Bungler & Cruden 2011). For the case of constant-rate injection into weak rock, with vapour occupying only a small proportion of the tip, we find the radial extent increases like $t^{4/13}$ up to the elastogravity length scale $(B/\rho g)^{1/4}$ and $t^{4/17}$ beyond it. In future work it would be interesting to reappraise the geological data in comparison with these and other spreading regimes.

A novel feature of the solutions in §4 is the presence of a region of dry shear failure ahead of the fluid front, with extent comparable to the $O(d)$ thickness of the overlying sheet. This possibility is a consequence of the mixed-mode loading of the crack tip which arises from asymmetry between the finite-thickness sheet and the semi-infinite substrate. Since the crack is confined to a planar interface, the shear loading of the tip cannot be alleviated simply by kinking or curving away from the initial crack plane (cf., e.g., Cotterell & Rice 1980; Meriaux & Lister 2002). Geologically, evidence for such shear failure might be sought in a dry joint ahead of the magmatic tip.

We have focused on the simplest problem that demonstrates our main point, that the full equations of elasticity provide a way to resolve the apparent elastic contact-line problem in beam theory. As a result, our solutions effectively have just a single parameter describing the strength of any bonding. In the course of the analysis, a number of extensions to the simple problem have been suggested for future work. These include allowing some fluid lag, adding a significant tension to the remote bending moment, having friction on any region of shear failure, and allowing the sheet and substrate to have different elastic properties. While these complicate the problem, we anticipate that the physical ideas elucidated in this paper will remain central.

DJS was supported by the Engineering and Physical Sciences Research Council under the UROP scheme. TMJL was supported by a summer studentship from Trinity College, Cambridge. All data accompanying this publication are directly available within the publication.

Appendix A. Numerical schemes

A.1. Fluid-filled crack

We discretized the problem (2.10)–(2.12) by taking $n + 1$ points ξ_i , $i = 0, \dots, n$, at which to represent H' and G' . We used a set of points of the form

$$\xi_i = \tan^2(\phi i/m), \quad i = 1, \dots, m < n \quad (\text{A } 1)$$

$$\xi_i = (\xi_m/\xi_{m-1})\xi_{i-1}, \quad i = m + 1, \dots, n, \quad (\text{A } 2)$$

where ϕ and m were such that $\xi_m = O(10)$ and $\xi_n = O(10^3)$. This was chosen so that points are concentrated in a square-root manner in the important region near the tip, and spread out in a geometric progression in the far-field $\xi \gg 1$, but it is otherwise fairly arbitrary.

For each interval $\xi_{i-1} < \xi < \xi_i$, we interpolated H' and G' using

$$\xi^{1/2}G'(\xi) = a_i\xi + b_i, \quad \xi^{1/2}H'(\xi) = c_i\xi + d_i, \quad i = 1, \dots, t \quad (\text{A } 3)$$

$$G'(\xi) = a_i\xi + b_i, \quad H'(\xi) = c_i\xi + d_i, \quad i = t + 1, \dots, n \quad (\text{A } 4)$$

The two sets of interpolating functions were chosen to represent the functional forms for $\xi \ll 1$ and $\xi \gg 1$, but the division point $t \approx n/2$ is fairly arbitrary. These interpolating functions allow the integrals in (2.10) and (2.11) to be performed analytically. We also need to extrapolate to $\xi > \xi_n$ to complete the integrals, and continued to use a piecewise linear representation of H' and G' for simplicity, with slopes H'' and G'' given by

$$a_{n+1} = \frac{G''_\infty(\xi_n)}{G'_\infty(\xi_n)}G'_n, \quad c_{n+1} = \frac{H''_\infty(\xi_n)}{H''_\infty(\xi_{n-1})}c_n, \quad (\text{A } 5)$$

where H''_∞ and G'_∞ are given by the asymptotic form (2.15).

We define a vector of $2(n+1)$ unknowns $\boldsymbol{\theta} = [\sqrt{\xi_0}H'(\xi_0), \dots, \sqrt{\xi_t}H'(\xi_t), H'(\xi_{t+1}), \dots, H'(\xi_n), \sqrt{\xi_0}G'(\xi_0), \dots, \sqrt{\xi_t}G'(\xi_t), G'(\xi_{t+1}), \dots, G'(\xi_n)]$, from which one can easily determine the interpolation, and thence evaluate the two components of the elasticity integral (2.10) at n intervening points $\xi_{1/2}, \dots, \xi_{n-1/2}$. Using the linearity of these operations, we can thus define a square matrix \mathbf{A} such that

$$[P(\xi_{1/2}), \dots, P(\xi_{n-1/2}), \underbrace{0, \dots, 0}_n, G'(\xi_n), H''(\xi_n)] = \mathbf{A}\boldsymbol{\theta}. \quad (\text{A } 6)$$

One can obtain analytical expressions for $H(\xi)$ by integrating the representation of H' , and then for $P(\xi)$ by integrating H^{-2} in (2.11). Let $\mathbf{p}(\boldsymbol{\theta})$ denote the vector of values found by evaluating $P(\xi_{i-1/2})$, $i = 1, \dots, n$, in this way. Equating the two expressions for P and using the asymptotic conditions (2.15), we obtain the equation

$$\mathbf{A}\boldsymbol{\theta} = [\mathbf{p}(\boldsymbol{\theta}), \underbrace{0, \dots, 0}_n, G'_\infty(\xi_n), H''_\infty(\xi_n)]. \quad (\text{A } 7)$$

which can be solved by Newton's method from quite arbitrary initial guesses. The accuracy of the numerical results was checked by varying the parameters of the discretization; the main considerations are that n and ξ_n should be sufficiently large.

A.2. Linear perturbation problem

For the linear perturbation problem in appendix B, we anticipate a singularity of the form ξ^{s-1} in \tilde{H}' , with $s = 0.139$, and the weighting in the interpolation (A 3) was changed to reflect this. (We still expect \tilde{G}' to have a $\xi^{-1/2}$ singularity.) Some of the

integrals no longer have exact expressions, but can be carefully pre-calculated for the relevant intervals by numerical integration.

The lubrication equation (B 8b) for the perturbation problem is linear in \tilde{H} . Therefore, the function $\tilde{p}(\tilde{\theta})$ appearing in the equation analogous to (A 7) is linear, and we can solve this equation directly without recourse to Newton's method.

The zero-toughness solution H_0 was obtained by extrapolation with respect to k_I for each $\xi_i > 0.002$. (Figure 4 shows that, away from the boundary layer near $\xi = 0$, $H'(\xi)$ for $k_I = 0.21$ is already a good approximation to H'_0 .) For $\xi_i < 0.002$ the linear trend in $0.002 < \xi < 0.003$ was simply extended to $\xi = 0$.

A.3. Dry cracking ahead of the fluid

To solve the problem in §4.1 of dry shear failure at $\xi = -L$ preceding a fluid front at $\xi = 0$, we adapted the scheme for §3 by adding more points to cover the interval $-L \leq \xi < 0$. The spacing of points for $\xi < 0$ was chosen such that there was a concentration of points near $-L$ and near 0.

We also adapted the interpolation of G' from (A 3a) to reflect the $(\xi+L)^{-1/2}$ singularity at $\xi = -L$, while continuing to allow H' to have a $\xi^{-1/2}$ singularity at $\xi = 0$ for the solutions with $k_I \neq 0$. Since $H' = 0$ in $\xi < 0$, we did not need to calculate P for $\xi < 0$ (although it is easily done): simply requiring that $\sigma_{xy} = 0$ at the intervening points in $\xi < 0$ provides enough additional equations to determine G' in $-L \leq \xi < 0$. The problem can then be solved as before with Newton's method.

Appendix B. Small toughness solution

In this appendix, we show how to predict the behaviour seen in figure 3 as $k_I \rightarrow 0$ (or $V \rightarrow V_0$). Let H_0 , G_0 , P_0 and V_0 be the solution of (2.10)–(2.13) for $k_I = 0$, with the asymptotic behaviour (3.2) as $\xi \rightarrow 0$. (The behaviour $G'_0 \sim (k_{II}/\chi)\xi^{-1/2}$ is not relevant to the following analysis.) We assume that for $k_I \ll 1$ and away from $\xi = 0$, we can set up a perturbation expansion of the form

$$\begin{aligned} H(\xi) &= H_0(\xi) + \epsilon(k_I)H_1(\xi) + \dots \\ G(\xi) &= G_0(\xi) + \epsilon(k_I)G_1(\xi) + \dots \\ P(\xi) &= P_0(\xi) + \epsilon(k_I)P_1(\xi) + \dots \\ V &= V_0 + \epsilon(k_I)V_1 + \dots, \end{aligned} \tag{B 1}$$

with a small parameter ϵ .

Near $\xi = 0$ this expansion must break down, because $H \sim k_I \xi^{1/2}$ is much larger than $H_0 \sim V_0^{1/3} \xi^{2/3}$. The balance $k_I \xi^{1/2} \sim V^{1/3} \xi^{2/3}$ suggests the rescaling, with some convenient numerical factors,

$$\xi = \kappa^6 \psi^{-2} \hat{\xi}, \quad H = \kappa^4 \psi^{-1} \hat{H}, \quad P = \psi \kappa^{-2} \hat{P}, \quad \text{where} \quad \psi = 12V, \quad \kappa = (32/\pi)^{1/2} k_I. \tag{B 2}$$

In the rescaled variables, equations (3.1), (2.11) and (2.13) become

$$\hat{P}(\hat{\xi}) = \frac{1}{4\pi} \int_0^\infty \frac{\hat{H}'(\tilde{\xi})}{\tilde{\xi} - \hat{\xi}}, \quad \hat{H}^2 \hat{P}' = 1, \quad \hat{H} \sim \hat{\xi}^{1/2} \text{ as } \hat{\xi} \rightarrow 0, \tag{B 3}$$

which are the same as the small-toughness boundary-layer equations derived and solved numerically by Garagash & Detournay (2005) in the context of a different problem. They showed that

$$\hat{H} \sim \beta \hat{\xi}^{2/3} + \beta_1 \hat{\xi}^s \quad \text{as} \quad \hat{\xi} \rightarrow \infty \tag{B 4}$$

where $\beta = 3(4/3)^{1/6}$, $\beta_1 = 0.03719$ and $s = 0.013867$. Reverting to the outer variables, we find that the matching condition for the outer solution is

$$H \sim b_1 V^{2s-1} k_I^{4-6s} \xi^s + 6(3V^2)^{1/6} \xi^{2/3} \quad \text{as } \xi \rightarrow 0, \quad (\text{B } 5)$$

where $b_1 = 0.2439$.

After comparing the expansion (B 1) with (B 5), we set $\epsilon = b_1 V_0^{2s-1} k_I^{4-6s}$ and write $V^{1/3} = V_0^{1/3}(1 + \epsilon V_1/3V_0 + \dots)$. On substituting the expansion into (2.10)–(2.13) and equating terms of order ϵ , we obtain the linear perturbation problem

$$\begin{bmatrix} P_1 \\ 0 \end{bmatrix} = \int_0^\infty \mathbf{K}(\xi - \tilde{\xi}) \begin{bmatrix} H'_1(\tilde{\xi}) \\ G'_1(\tilde{\xi}) \end{bmatrix} d\tilde{\xi}, \quad H_0^2 P'_1 + 2H_0 H_1 P'_0 = V_1, \quad (\text{B } 6)$$

$$H_1'' \rightarrow 0 \text{ as } \xi \rightarrow \infty, \quad H_1 \sim \xi^s + \frac{V_1}{3V_0} H_0(\xi) + \dots \text{ as } \xi \rightarrow 0. \quad (\text{B } 7a, b)$$

These equations determine the value of V_1 through the condition that the perturbed propagation speed is consistent with no perturbation to the far-field forcing $H'' \rightarrow 12$.

For numerical solution, it is convenient to subtract $V_1/3V_0$ times the zero-toughness solution to simplify (B 7b), and then rescale to obtain

$$\begin{bmatrix} \tilde{P} \\ 0 \end{bmatrix} = \int_0^\infty \mathbf{K}(\xi - \tilde{\xi}) \begin{bmatrix} \tilde{H}'(\tilde{\xi}) \\ \tilde{G}'(\tilde{\xi}) \end{bmatrix} d\tilde{\xi}, \quad H_0^2 \tilde{P}' + 2H_0 \tilde{H} P'_0 = 0, \quad (\text{B } 8)$$

$$\tilde{H}'' \rightarrow 12 \text{ as } \xi \rightarrow \infty, \quad \tilde{H} \sim \gamma \xi^s + \dots \text{ as } \xi \rightarrow 0. \quad (\text{B } 9)$$

where $\gamma = -3V_0/V_1$, and $\tilde{H} = \gamma[H_1 - (V_1/3V_0)H_0]$ etc.

Equations (B 8) and (B 9) were solved numerically as described in appendix A. We find that $\gamma = 6.91$ and hence $V_1 = -14.0$. The final asymptotic result

$$V \sim V_0 - (3b_1/\gamma) V_0^{2s} k_I^{4-6s} = 0.678 - 0.0950 k_I^{4-6s} \quad \text{as } k_I \rightarrow 0$$

shows excellent agreement with the results from the full numerical calculations (figure 5), providing a check both on the numerical calculations and on the understanding of the boundary-layer structure. The asymptotic result is also useful for moderately small k_I since it gives an excellent prediction of the speed of propagation without having to resolve the very thin $O(k_I^6)$ boundary-layer structure.

REFERENCES

- BALL, T. V. & NEUFELD, J. A. 2018 Static and dynamic fluid-driven fracturing of adhered elastica. *Phys. Rev. Fluids* **7**, 074101.
- BONN, D., EGGERS, J., INDEKEU, J., MEUNIER, J. & ROLLEY, E. 2009 Wetting and spreading. *Rev. Mod. Phys.* **81**, 739–805.
- BUNGER, A. P. & DETOURNAY, E. 2005 Asymptotic solution for a penny-shaped near-surface hydraulic fracture. *Eng. Fracture Mech.* **72**, 2468–2486.
- BUNGER, A. P. & CRUDEN, A. R. 2011 Modelling the growth of laccoliths and large mafic sills: Role of magma body forces. *J. Geophys. Res.* **116**, B02203 (and correction B08211).
- COTTERELL B. & RICE, J.R. 1980 Slightly curved or kinked cracks. *Intl. J. Fracture*, **16**, 155–169.
- CHOPIN, J., VELLA, D. & BOUDAUD, A. 2008 The liquid blister test. *Proc. R. Soc. A* **464**, 2887–2906.
- DESROCHES, J., DETOURNAY, E., LENOACH, B., PAPANASTASIOU, P., PEARSON, J. R. A., THIERCELIN, M. & CHENG, A. 1994 The crack tip region in hydraulic fracturing. *Proc. R. Soc. Lond. A*, **400**, 39–48.
- DETOURNAY, E. 2016 Mechanics of hydraulic fractures. *Annu. Rev. Fluid Mech.* **48**, 311–339.
- DUCLOUÉ, L., HAZEL, A. L., THOMPSON, A. B., JUEL, A. 2017 Reopening modes of a collapsed elasto-rigid channel. *J. Fluid Mech.* **819**, 121–146.
- DYSKIN, A. V., GERMANOVICH, L. N. & USTINOV, K. B. 2000 Asymptotic analysis of crack interaction with free boundary. *Intl. J. Solids and Structures* **37**, 857–886.
- FLITTON, J. C. & KING, J. R. 2004 Moving-boundary and fixed-domain problems for a sixth-order thin-film equation. *Euro. J. Appl. Math.* **15**, 713–754.
- GARAGASH, D. I. & DETOURNAY, E. 2000 The tip region of a fluid-driven fracture in an elastic medium. *J. Appl. Mech.* **67**, 183–192.
- GARAGASH, D. I. & DETOURNAY, E. 2005 Plane-strain propagation of a fluid-driven fracture: small toughness solution. *J. Appl. Mech.* **72**, 916–928.
- GOMEZ, M., MOULTON, D. E. & VELLA, D. 2017 Passive control of viscous flow via elastic snap-through. *Phys. Rev. Lett.* **119**, 144502.
- GROTBERG, J. B. & JENSEN, O. E. 2004 Biofluid mechanics in flexible tubes. *Annu. Rev. Fluid Mech.* **36**, 121–147.
- HEAD, A. K. 1953 Edge dislocations in inhomogeneous media. *Proc. Phys. Soc. Lond B* **66**, 793–800.
- HEIL, M. & HAZEL, A. 2011 Fluid-structure interaction in internal physiological flows. *Ann. Rev. Fluid Mech.* **43**, 141–162.
- HERVET, H. & DE GENNES, P.-G. 1984 The dynamics of wetting: Precursor films in the wetting of “dry” solids. *C. R. Acad. Sci., Ser. II* **299**, 499–503.
- HEWITT, I. J., BALMFORTH, N. J. & DE BRUYN, J. R. 2015 Elastic-plated gravity currents. *Eur. J. Appl. Math.* **26**, 1–31.
- HOCKING, L. M. 1983 The spreading of a thin drop by gravity and capillarity. *Quart. J. Mech. Appl. Maths.*, **36**, 55–69.
- HODGES, S. R. & JENSEN, O. E. 2002 Spreading and peeling dynamics in a model of cell adhesion. *J. Fluid Mech.* **460**, 381–409.
- HOSOI, A. E. & MAHADEVAN, L. 2004 Peeling, healing, and bursting in a lubricated elastic sheet. *Phys. Rev. Lett.* **93**, 137802.
- JENSEN, O. E., HORSBURGH, M. K., HALPERN, D., GAVER, D. P. 2002. The steady propagation of a bubble in a flexible-walled channel: Asymptotic and computational models. *Phys. Fluids*. **14**, 443–57
- JENSEN, H. M., HUTCHINSON, J. W. & KIM, K.-S. 1990 Decohesion of a cut prestressed film on a substrate. *Int. J. Solids Structures* **26**, 1099–1114.
- JENSEN, H. M. 1991 The blister test for interface toughness measurement. *Engng. Fracture Mech.* **40**, 475–486.
- KAVANAGH, J. L., ROGERS, B. D., BOUTELIER, D. & CRUDEN, A. R. 2017 Controls on sill and dyke-sill hybrid geometry and propagation in the crust: The role of fracture toughness. *Tectonophysics* **698**, 109–120.
- KANNINEN, M. F. & POPELAR, C. H. 1985 *Advanced fracture mechanics*. Oxford.

- LEAL, L. G. 1992. *Laminar flow and convective transport processes*. Butterworth-Heinemann.
- LISTER, J. R. 1990 Buoyancy-driven fluid fracture: the effects of material toughness and of low viscosity precursors. *J. Fluid Mech.* **210**, 263–280.
- LISTER, J. R., PENG, G. G. & NEUFELD, J. A. 2013 Viscous control of peeling an elastic sheet by bending and pulling. *Phys. Rev. Lett.* **111**, 154501.
- LEONG, F. Y. & CHIAM, K.-H. 2010 Adhesive dynamics of lubricated films. *Phys. Rev. E* **81**, 041923.
- MCEWAN, A. D. & TAYLOR, G. I. 1966 The peeling of a flexible strip attached by a viscous adhesive. *J. Fluid Mech.* **26**, 1–15.
- MERIAUX, C. & LISTER, J. R. 2002 Calculation of dyke trajectories from volcanic centres. *J. Geophys. Res.* **107**, 10.129/2001JB000436.
- MICHAUT, C. 2011 Dynamics of magmatic intrusions in the upper crust: Theory and applications to laccoliths on Earth and the Moon. *J. Geophys. Res.* **116**, B05205.
- PENG, G. G. 2017 *Viscous flows under elastic sheets*. Ph.D. thesis, University of Cambridge.
- PENG, G. G., PIHLER-PUZOVIĆ, D., JUEL, A., HEIL, M. & LISTER, J. R. 2015 Displacement flows under elastic membranes. Part 2. Lubrication theory for two-phase flow. *J. Fluid Mech.* **784**, 512–547.
- PIHLER-PUZOVIĆ, D., ILLIEN, P., HEIL, M. & JUEL, A. 2012 Suppression of complex fingerlike patterns at the interface between air and a viscous fluid by elastic membranes. *Phys. Rev. Lett.* **108**, 074502.
- PIHLER-PUZOVIĆ, D., JUEL, A., PENG, G. G., LISTER, J. R. & HEIL, M. 2015 Displacement flows under elastic membranes. Part 1. Experiments and direct numerical simulations. *J. Fluid Mech.* **784**, 487–511.
- POLLARD, D. D. & JOHNSON, A. M. 1973 Mechanics of growth of some laccolithic intrusions in the Henry Mountains, Utah, I: Field observations, Gilbert's model, physical properties and flow of the magma. *Tectonophysics* **18**, 261–309.
- RICE, J. R. 1968 Mathematical analysis in the mechanics of fracture. In *Fracture, an advanced treatise. Vol. II* (ed. H. Liebowitz), 191–311. Academic Press.
- ROGERS, J. A., SOMEYA, T. & HUANG, Y. 2010 Materials and mechanics for stretchable electronics. *Science* **327**, 1603.
- SPENCE & SHARP 1985 Self-similar solutions for elastohydrodynamic cavity flow. *Proc. R. Soc. Lond. A*, **400**, 289–313.
- SUO, Z. & HUTCHINSON, J. W. 1990 Interface crack between two elastic layers. *Int. J. Fracture* **43**, 1–18.
- THOULESS, M. D., EVANS, A. G., ASHBY, M. F. & HUTCHINSON, J. W. 1987 The edge cracking and spalling of brittle plates. *Acta metall.* **35**, 1333–1341.
- WANG, Z.-Q. & DETOURNAY, E. 2018 The tip region of a near-surface hydraulic fracture. *J. Appl. Mech.* **85**, 041010.
- YANG, F. & LI, J. C. M. 1997 Dislocation model of a subsurface crack. *J. Appl. Phys.* **82**, 4816–4822.
- YUUKI, R., LIU, J.-Q., OHIRA, T. & ONO, T. 1994 Mixed mode fracture for an interface crack. *Engng Fracture Mech.* **47**, 367–377.
- ZHANG, X., DETOURNAY, E. & JEFFREY, R. G. 2002 Propagation of a penny-shaped hydraulic fracture parallel to the free-surface of an elastic half-space. *Int. J. Fracture* **115**, 125–158.
- ZHANG, X., JEFFREY, R. G. & DETOURNAY, E. 2005 Propagation of a hydraulic fracture parallel to a free surface. *Int. J. Numer. Anal. Meth. Geomech.* **29**, 1317–1340.
- ZLATIN, A. H. & KHRAPKOV, A. A. 1986 A semi-infinite crack parallel to the boundary of the elastic half-plane. *Dokl. Akad. Nauk SSSR.* **31**, 1009–1010.